Magnetically Controlled Modular Cubes With Reconfigurable Self-Assembly and Disassembly

Anuruddha Bhattacharjee, Yitong Lu, Aaron T. Becker, *Senior Member, IEEE*, and MinJun Kim, *Senior Member, IEEE*

***Abstract*—Reconfigurable modular robots, which can actively assemble and disassemble on command, offer the possibility of mesoscale (milliscale and microscale) manufacturing with robustness and controllability. In this study, we present a design of a scalable modular subunit with embedded permanent magnets in a 3-D printed cubic body. The subunit can be wirelessly controlled by an external uniform magnetic field. We also present controlled assembly–disassembly techniques for these subunits. Our modular robotic platform is highly reconfigurable and can create programmable, predetermined patterns based on open-loop control. The 2-D motion planner computes all reachable polyomino shapes from an arbitrary initial configuration and provides the shortest movement sequences to form each shape. Experimental results match computational modeling, demonstrating robust and reproducible behavior of the modular robotic platform that is promising for mesoscale manufacturing applications. Two cube sizes were tested: 10-mm edge lengths and 2.8-mm edge lengths.**

***Index Terms*—Self-assembly, Multi-robot systems, Motion planning, Path planning.**

I. Introduction

RECONFIGURABLE modular self-assembly is a promising approach for manufacturing. Self-assembly processes are also ubiquitous in nature, as they generate most of the functionality in living organisms [1]. The key to self-assembly is that the functional information encoded in the design of the building blocks or modular subunits determines the interactions that organize them into desired patterns. While conventional fixed-structure manipulators have a static design, modular manipulators can reconfigure to meet time-varying task requirements. This article presents the magnetic modular cubes shown in Fig. 1. A key quality is that the resulting structure is *itself* a large robot that can move in or manipulate its environment or can be reconfigured to optimize for tasks including movement, encapsulation, or manipulation, as shown by these applications.

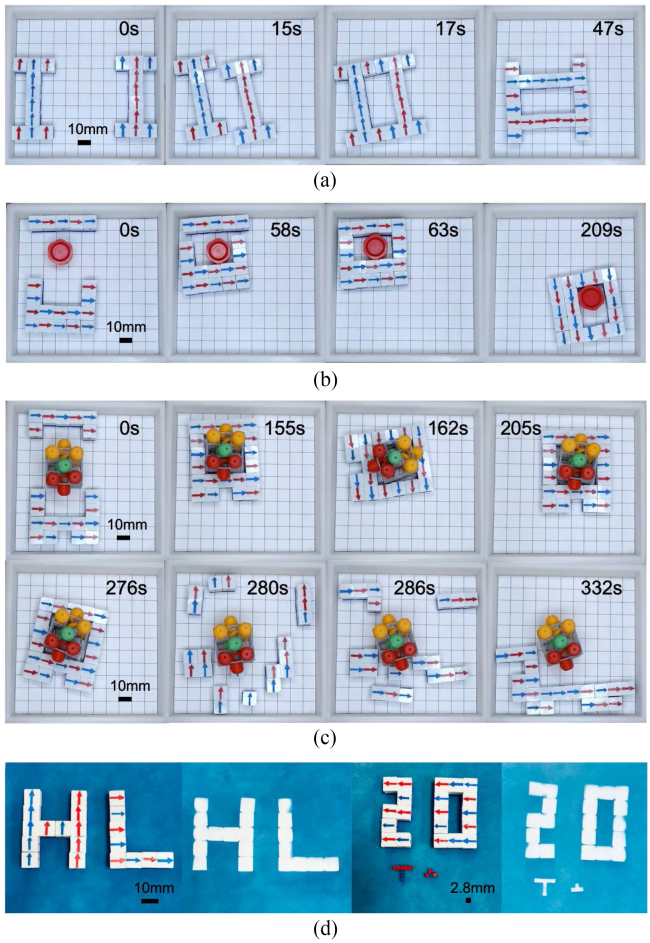

Fig. 1. Modular cubes with embedded magnets can be actuated in unison by an external magnetic field to move, assemble, and disassemble. Collisions with boundaries enable reconfiguring the cubes. The embedded magnets encode which cubes can bond. Four potential applications are shown: (a) Combining two 10-cube robots into a 20-cube mobile structure. (b) Assembling to manipulate a nonmagnetic object. (c) Assembling, disassembling, and reassembling to manipulate a 3-D printed toy. (d) Lithography using photo paper and modular cubes as reconfigurable masks. See the attachment for videos of these demonstrations.

Modular design can improve the flexibility, scalability, maintainability, and interchangeability of systems, increasing the number of applications for the system and enabling reuse [2]. Modular reconfigurable robots have a specific advantage over

Manuscript received May 6, 2021; revised August 24, 2021; accepted September 12, 2021. National Science Foundation under Grants Nos. IIS-2130775, 2130793, 1553063, 1712088, CMMI-1712096, and CNS-1932572. This paper was recommended for publication by Associate Editor L. Zhang and Editor M. Yim upon evaluation of the reviewers' comments. *(Anuruddha Bhattacharjee and Yitong Lu contributed equally to this work.) (Corresponding authors: Aaron T. Becker; MinJun Kim.)*

Anuruddha Bhattacharjee and MinJun Kim are with the Department of Mechanical Engineering, Southern Methodist University, Dallas, TX 75205 USA (e-mail: abhattacharjee@smu.edu; mjkim@lyle.smu.edu).

Yitong Lu and Aaron T. Becker are with the Department of Electrical and Computer Engineering, University of Houston, Houston, TX 77204 USA (e-mail: ylu36@uh.edu; atbecker@central.uh.edu).

This article has supplementary material provided by the authors and color versions of one or more figures available at https://doi.org/10.1109/TRO.2021.3114607.

Digital Object Identifier 10.1109/TRO.2021.3114607

traditional robotic platforms in terms of ease in manufacturing, as the modular design allows the robots to dynamically assemble/disassemble as required with less human intervention [3]. Moreover, the reconfiguration capability of the robots enables them to dynamically adapt to uncertain environments [4]. Recent advances in self-reconfiguring swarm robotics and particle computation have shown great promise for future applications in targeted drug delivery, drug screening, and mesoscale (milliscale and microscale) manufacturing [2], [5]–[10]. For example, modular assembly/disassembly of particles might enhance the efficiency of drug delivery. Aggregating the particles gives the assembly more power, enabling deeper penetration and faster propagation, while disassembling the particles increases surface area to improve drug release [5]. On the other hand, a swarm of modular robots can reconfigure themselves through targeted assembly–disassembly to fabricate different tools that could be useful for complex mesoscale manufacturing [10].

Reconfigurable modular robots usually contain sensors and mechanisms for motion (actuation) and connection; however, in most cases, the motion and connection systems are the heaviest and consume the most energy-limiting scalability of modules [11]. Hence, it is advantageous to use a system that combines motion and coupling. A magnetic motion and coupling system is a competitive choice due to its versatility, flexibility, and stability of control. Adopting magnetic coupling can eliminate the need for on-board actuators and other mechanical elements, making magnetic docking methods particularly helpful in mesoscale applications [12]. Moreover, the magnetic fields used to actuate can easily and harmlessly permeate most biological and synthetic materials [7], [13], making them safe for real-world applications.

In the last few decades, many research projects have been conducted based on magnetic actuation [14] and coupling systems [12] to explore reconfigurable modular robotics and self-assembly at different length scales, such as macroscale [15]–[20], milliscale [21]–[24], and microscale [5], [9], [25], [26]. Researchers have developed modules with excellent locomotion and manipulation abilities and have integrated advanced control algorithms (swarm intelligence, self-organization, etc.) that enable accurate motion and good dynamic performance [26]. Several reconfiguration strategies of modules, such as autonomous and distributed stochastic self-assembly [16], self-reconfiguration by rotation in a planar workspace [15], [27], locomotion through reconfiguration on a cubic lattice [28], [29], and universal and distributed reconfiguration planning for square and hexagonal lattice based robots [30] have been investigated. However, the computational cost of reconfiguration planning in a modular robotic platform increases exponentially with the number of modules [31]. Moreover, some systems use complex decoupling mechanisms [19], [20], [32], which raise uncertainty for their functionality in a dynamic system. Although a few magnetic modular platforms could achieve precise control [23] (through electrostatic anchoring) and stable assembly performance [22] (by tuning the magnetic dipole moment) of subunits, deterministic disassembly and reassembly toward a successful reconfiguration is still an unsolved problem. Therefore, there is a need for *robust*, *scalable*, *controllable*, and *efficient* methods to overcome the existent issues regarding modular robotics and self-reconfiguration. This article represents a step in that direction.

This article reports a design of a scalable modular robotic platform and techniques for controlled self-assembly, disassembly, and reassembly with computational modeling and experimental validation. Our modular subunits have 3-D printed cubic bodies with embedded permanent magnets, can be wirelessly controlled by an external uniform magnetic field and actuated using two motion modes (pivot walking [33]–[35] and rolling motion [36]), are dynamically reconfigurable, and can assemble into desired shapes by following open-loop magnetic control inputs. Our experimental results show that the motion mechanism and assembly–disassembly techniques of the modular robotic platform are controllable and reproducible, which is promising for practical applications. This combination of modular cubes with preferential binding affinities coded by embedded magnets and global control sequences for self-assembly and disassembly could be used to simplify and upgrade the capabilities of existing mesoscale manufacturing technologies.

II. Materials and Methods

A. Design and Fabrication Process of Magnetic Modular Subunits and Experimental Workspace

Individual cubes with 10- and 2.8-mm edges as well as the experimental workspace were designed using computer-aided design (CAD) software (Onshape). Fig. 2 shows the CAD models of different parts of the modular cube design with 10- and 2.8-mm edges, a cylindrical micromagnet, and the experimental workspace. As shown in Fig. 2(a), the modular subunit design with 10-mm edges includes two parts: the top cover and the core body with eight holes in four faces for embedding permanent magnets. The two parts were 3-D printed (using an Ultimaker 2 Extended+) separately using polylactic acid. After finishing the 3-D printing process, eight cylindrical permanent magnets (each having a diameter and a height of 1.6 mm, nickel-coated, with a strength of Neodymium 50) were embedded in the holes with a specific orientation of north/south poles [as shown in Fig. 3(b)]. The dimensions are set with tolerances that follow the specifications of the 3-D printer. Finally, a top cover was attached to finish the fabrication of a modular subunit. The top cover is used to prevent the magnets from coming out of the holes as well as to prevent them from aggregating internally.

The scaled-down version of the modular cube subunit with 2.8-mm edges was printed using Projection Micro Stereolithography (P μ SL) 3-D printing by Empire Group USA (a commercial partner of Boston Micro Fabrication). The 3-D printer used can achieve a layer resolution of 2 μm, is facilitated with a UV-LED (405 nm) light source, and uses a photosensitive resin as the printing material. The dimensions of the modular cube subunit, as shown in Fig. 2(b), are set based on the tolerance of the 3-D printer and the dimensions of the smallest commercially available cylindrical micromagnet [Fig. 2(c)]. After collecting the 3-D printed cubes, eight micromagnets (each having a diameter of 0.3 mm and a height of 0.5 mm, nickel-coated, with a strength of Neodymium 52) were embedded in the holes using Gorilla super glue.

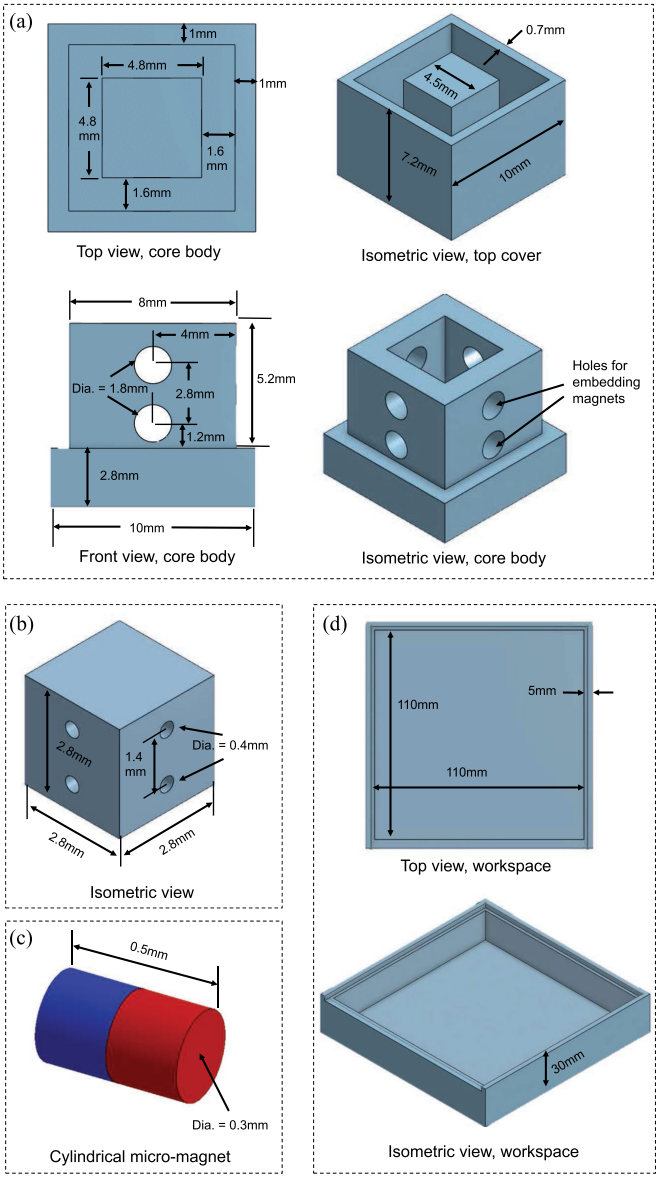

Fig. 2. 3-D CAD models. (a) Schematics showing the two parts of a modular cube subunit with 10-mm edges (i.e., core body and top cover). The top, front, and isometric views represent the core body of a modular cube design that is 3-D printed along with the top cover (isometric view) and assembled with eight embedded permanent magnets to create a magnetic modular subunit. (b) Schematic showing the isometric view of modular cube subunit with 2.8-mm edges. (c) 3-D model of an axially magnetized cylindrical micromagnet. (d) Top and isometric views of the experimental workspace.

A workspace with a boundary wall [Fig. 2(d)] was designed and 3-D printed to perform experiments inside the nested Helmholtz coil system (see Section II-C). The boundary of the workspace plays a vital role in the assembly process of modular subunits by breaking the motion symmetry of individual modular subunits. This symmetry-breaking enables controlling multiple subunits with one global control input.

B. Motion Modes

Fig. 3(a) shows the reference coordinate systems (XYZ) for the external magnetic field and the modular cube subunit, where α and ψ are pitch angles, and θ and ϕ are yaw angles. The yaw angle is defined as the angle from the X-axis to the vector projection into the horizontal plane ($X-Y$ plane), and the pitch angle is defined as the angle from the $X-Y$ projection to the vector. Fig. 3(b) shows two design variations of the magnetic modular subunits for cubes with 10- and 2.8-mm edges. Eight axially magnetized permanent magnets (two magnets per face) are embedded in the four faces of the cube, where three faces have the same magnetic orientation (north pole/south pole outward) and the other face has the opposite. The red/blue arrows on the top faces indicate the direction from magnetic south pole to north pole or, equivalently, the direction of the net magnetic moment. Cubes with blue arrows on the top faces are defined as blue cubes, and cubes with red arrows are defined as red cubes. When an external magnetic field is applied to create a pitch angle, the resultant magnetic flux density (B) makes an angle α with the $X-Y$ plane [Fig. 3(a)], which imposes a magnetic torque τ_x on the modular cube subunit along the x-axis of its body-fixed reference frame (xyz) [Fig. 3(b)]. This torque lifts part of the modular cube from the ground and keeps it tilted with a pitch angle ψ. Similarly, a yaw rotation can be achieved with the external magnetic field by generating B at an angle θ with the X-axis and along the $X-Y$ plane [Fig. 3(a)]. A yaw rotation created by the external magnetic field imposes a rotational torque τ_z on the modular cube subunit along the z-axis [Fig. 3(b)]. Alternate magnetization schemes are discussed in [37].

Embedded permanent magnets with a specific orientation in the cubes enable them to be actuated and controlled under an external magnetic control system through discrete motions, such as rolling [Fig. 3(c)] and pivot walking [Fig. 3(d)]. A 360° rotation of the modular cube's body completes one cycle of the rolling motion, where the rotation is achieved by four 90° steps of the applied magnetic torque τ_x. The pivot walking motion is achieved by six discrete steps, as shown schematically in Fig. 3(d) and experimentally in Fig. 4(a). The first step imposes a pivoting edge by lifting the modular cube's body with a counterclockwise rotational torque (τ_x) and holds the modular cube's body at a tilt with pitch angle ψ. The second step involves a clockwise yaw rotation of the modular cube by -$\phi/2$, which is achieved by a rotational torque -τ_z. The third step switches the pivoting edge by applying a clockwise torque (-τ_x) along the x-axis. The fourth step rotates the cube through a counterclockwise yaw of ϕ by applying a magnetic torque (τ_z) along the z-axis. Step five switches the pivoting edge back to the first edge. Step six rotates the cube by a yaw of $\phi/2$. These six steps complete one cycle of pivot walking motion.

Fig. 4(a) shows the six steps involved in one cycle of a pivot walking motion in the experiment. Before starting the cycle (at 0 s), the magnetic inputs are zero, and the net magnetic moment of the individual modular cubes are directed arbitrarily as placed in the workspace by a user. Six steps are performed with arbitrary time delays in between steps to keep the motion synchronized while capturing image data. Each magnetic torque is achieved by step inputs of a static magnetic field, as shown in Fig. 4(d). To perform a repeatability test of the pivot walking motion, ten experimental trials for each variation of the modular cubes (with 2.8- and with 10-mm edges) were

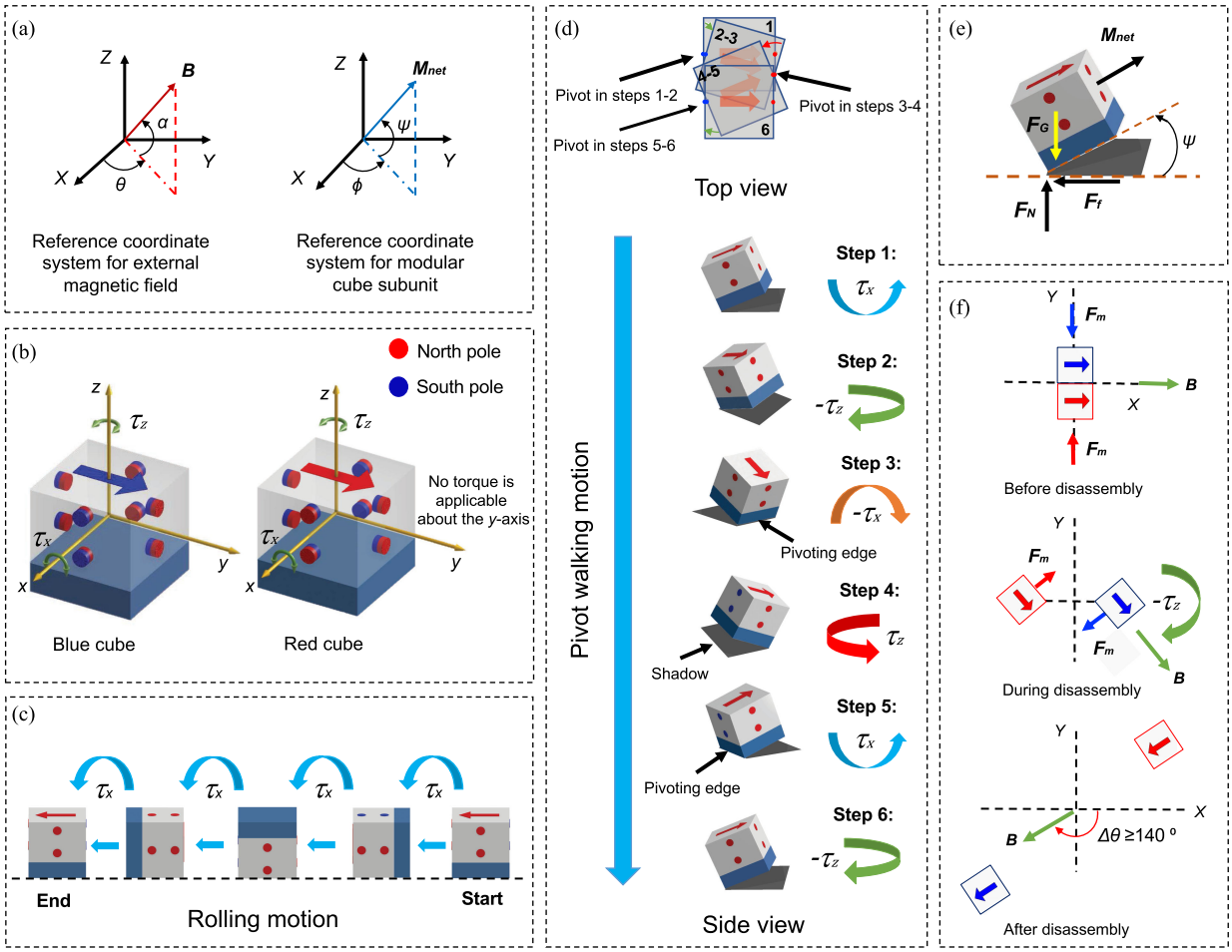

Fig. 3. (a) Schematic showing reference coordinate systems (XYZ) for external magnetic field and modular cube subunit. (b) Schematic showing the modular cube's body-fixed reference frame (xyz) with two design variations of modular subunits (i.e., blue cube and red cube). A design variation is achieved by embedding different combinations of eight permanent magnets in four faces of each cube. The magnets allow the modular cubes to rotate with only two rotational magnetic torques (i.e., τ_x and τ_z) along their body, fixed on the x- and z-axes, respectively. (c) Side view showing rolling motion of a modular cube subunit. (d) Top and side views of a modular cube subunit performing a cycle of pivot walking motion following six steps. (e) Free-body diagram of a modular subunit showing surface normal force (F_N), friction force (F_f), and gravitational force (F_G) acting on the modular cube, along with the direction of the net magnetic moment (M_{net}). (f) Disassembly mechanism of a structure of magnetic cubes, where F_m is the magnetic attraction force acting between the cubes.

performed. In each trial, the displacement after completing ten pivot walking cycles was recorded. The Euclidean displacement, X displacement, and Y displacement for the cubes with 2.8- and 10-mm edges are presented in the plots of Fig. 4(b) and (c). The average displacements with standard deviations per ten cycles of pivot walking are reported in plots with corresponding legends. The repeatability of pivot walking enables its use in open-loop control to actuate individual modular subunits while performing assembly experiments.

The equation governing the applied static magnetic field can be described by

$$B = \begin{bmatrix} B_X \\ B_Y \\ B_Z \end{bmatrix} = \begin{bmatrix} A\cos(\alpha)\cos(\theta) \\ A\cos(\alpha)\sin(\theta) \\ A\sin(\alpha) \end{bmatrix} \tag{1}$$

where B is the applied magnetic flux density, B_X, B_Y, and B_Z are the three-dimensional components along X-, Y-, and Z-axes, respectively, A is the amplitude, α is the pitch angle, and θ is the yaw angle, as shown in Fig. 3(a).

Under a uniform magnetic field with flux density B, a forceless magnetic torque ($\boldsymbol{\tau} = [\tau_x, 0, \tau_z]^\top$) is induced on the modular cube, which aligns the net magnetic moment (M_{net}) of the cube with the direction of the applied field. The applied torque can be calculated as follows:

$$\boldsymbol{\tau} = M_{\text{net}} \times B. \tag{2}$$

As $\boldsymbol{\tau}$ is always orthogonal to both M_{net} and B, it is impossible to generate a torque about the direction of M_{net}. This constrains torque generation on a dipole to two degrees of freedom, which is also evident in our modular cube model [Fig. 3(b)], where there is no active torque along the y-axis of the modular cube's body-fixed reference frame. When the magnetic field is applied at an angle α, the modular cube tilts at an angle ψ, as shown in Fig. 3(e). Although the angle ψ is generally smaller than the angle α, they become arbitrarily close with increased magnetic field magnitude.

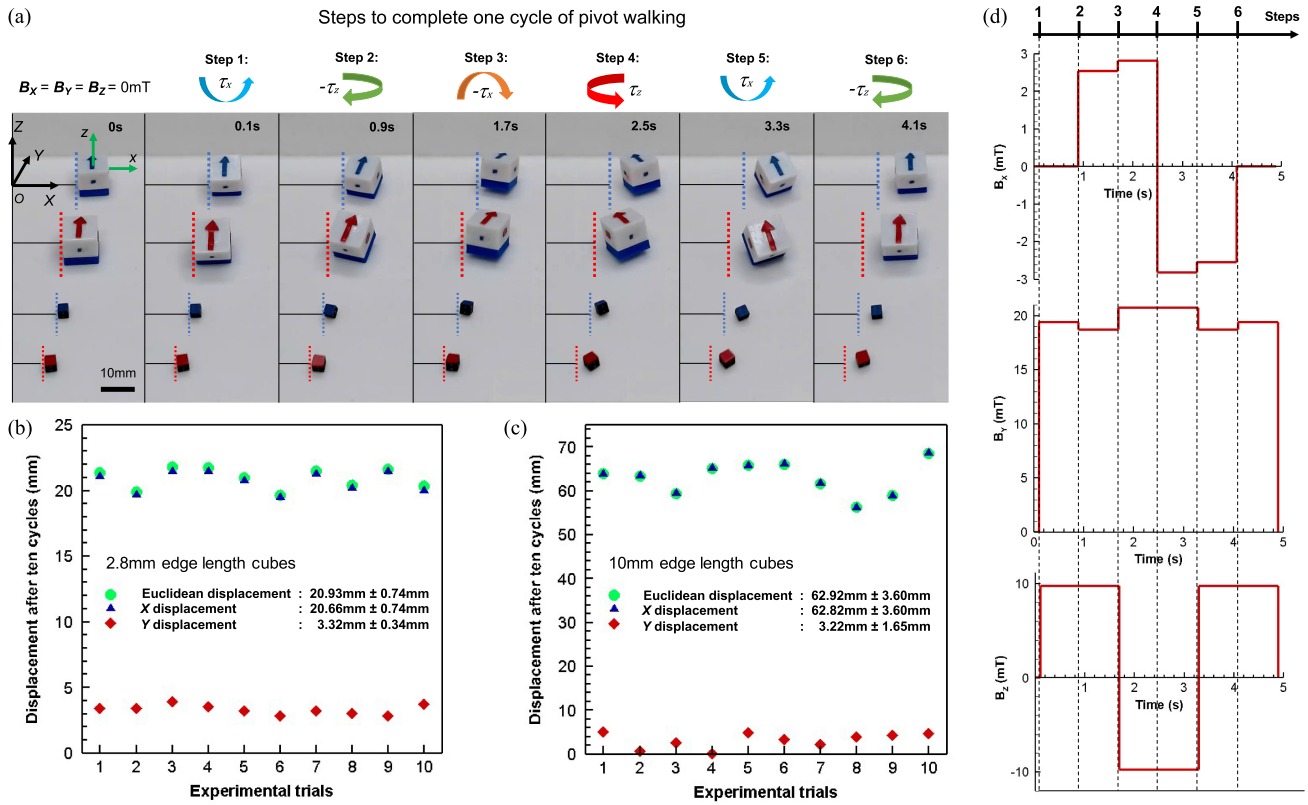

Fig. 4. (a) Video snapshots showing six steps in a cycle and the corresponding positions of four modular subunits to complete one cycle of the pivot walking motion. XYZ is the reference coordinate system and xyz is the modular cubes' body-fixed coordinate system with origins at point O and at the center of gravity of a modular cube, respectively. The dotted lines (red and blue) indicate position of a modular cube at 0 s (zero input). (b) Plots showing the Euclidean, X, and Y displacement of a modular cube with 2.8-mm edge after completing ten cycles of pivot walking motion in ten experimental trials. (c) Plots showing the Euclidean, X, and Y displacement of a modular cube with 10-mm edge after completing ten cycles of pivot walking motion in ten experimental trials. (d) Plots of external control inputs (magnetic flux density B_X, B_Y, and B_Z in X-, Y-, and Z-directions, respectively) with different time steps to create required torques (τ_x, -τ_x, τ_z, and -τ_z) for one cycle of pivot walking motion.

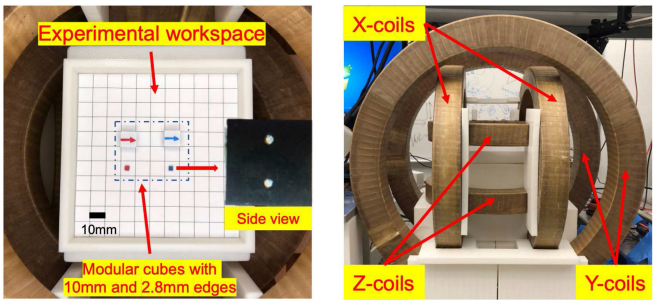

Fig. 5. (a) Top view of the experimental setup including core of the nested Helmholtz coil system, experimental workspace, four modular cubes with 10- and 2.8-mm edges, and a zoomed microscopic picture showing side view of a cube with 2.8-mm edge. (b) Front view of the nested Helmholtz coil system showing X-, Y-, and Z-coil pairs.

C. Experimental Setup and Nested Helmholtz Coil System

A large-scale nested, triaxial Helmholtz coil system was used to conduct experiments. Fig. 5(a) shows a top view of the experimental setup including the experimental workspace as well as modular cubes with 10- and 2.8-mm edges, while Fig. 5(b) shows a front view of the nested Helmholtz coil system. The nested Helmholtz coil system has three pairs of coils, which are labeled as X-coils, Y-coils, and Z-coils based on the centerlines of the coil pairs. Design specifications of the coil system are listed in [35]. The large size of the coils allows for a total working space of $150 \times 120 \times 80$ mm^3 at the center of the coil configuration. A magnetic field measurement probe (Metrolab THM1176-HFC-PC Teslameter) was used to measure magnetic flux density (mT) inside the coil system. All assembly–disassembly experiments were performed on the X–Y plane, where we assumed $Z = 0$ mm.

The coil system's large working distance and significant magnetic field strengths give modular robots ample space to maneuver and provide enough torque to produce described motion modes. Each coil pair is connected to its programmable power supply (Kepco, BOP 50-20 M), which is controlled by a National Instruments data acquisition (DAQ) board. The power supplies generate outputs to the coils, which in turn create a uniform static (or rotating) magnetic field with any user-specified, time-dependent magnitude and frequency. These signals are controlled using a customized C++ program; specific magnetic torque patterns for each coil pair are prespecified for individual motion modes.

III. Self-Assembly and Disassembly Behavior of Modular Cubes

Several experiments were conducted to explore modular self-assembly and disassembly techniques using sets of modular cubes. The external magnetic system can generate a flux density of more than 25 mT; however, a magnetic flux of 10 mT is enough to actuate the modular cubes toward successful assembly. Pivot walking motion is used in conjunction with the workspace boundary to actuate individual modular cubes with discrete motions, following predetermined paths to create a targeted assembly. When two or more modular cubes are self-assembled such that the arrows on their top face are aligned tip-to-tail, it is defined as a serial self-assembly. When the arrows are aligned side-by-side, it is defined as a parallel self-assembly.

Fig. 6(a) shows self-assembly and disassembly behavior of six modular cubes. The cubes were initially assembled into three groups. First, the three groups were gradually self-assembled to make a larger structure (at 28 s). Then, the assembled structure was partially disassembled by 14 mT into three groups at 33 s. Because red–blue bonds in serial (with arrows on their top faces aligned tip-to-tail) are stronger than other magnetic bonds, the structure disassembles into pairs of red–blue cubes connected in serial. Then the cubes were self-assembled into a long chain-like structure at 50 s and were gradually disassembled to six individual modular cubes (at 68 s). The magnetic flux density for disassembly was 22 mT, which resulted in a complete disassembly.

Starting with two groups of modular subunits, with an equal number of modular cubes in each group, two identical shapes [at 18 s in Fig. 6(b)], mirror shapes [at 23 s in Fig. 6(c)], and nonidentical shapes [at 20 s in Fig. 6(d)] could be created. The combination of modular subunits in each group can affect the final assembled shapes. As shown in Fig. 6(b) (at 0 s), the experiment starts with two identical groups and ends with two identical assembled shapes (at 18 s); whereas in Fig. 6(c) (at 0 s), starting with a different combination of subunits in one of the groups resulted in two mirror shapes of subassemblies (at 23 s). The subassemblies can be reassembled (at 32 s) after a partial disassembly and reconfiguration. When two mirror shapes were brought in close proximity (at 27 s), the blue cube in the left mirror shape was repulsed by the blue cube parallel to it and attracted by the blue cube serial to it. This situation in conjunction with the global inputs for pivot walking created an instability in the right mirror shape; therefore, the two blue cubes in serial assembled and resulted in the two reconfigured structures shown at 28 s. These were combined and the assembled structure was actuated by pivot walking (from 32 s to 34 s). Fig. 6(d) shows that it is also possible to create subassemblies of nonidentical shapes (at 20 s) starting from two identical groups of modules by an appropriate control sequence. The final configuration is determined by the control sequence.

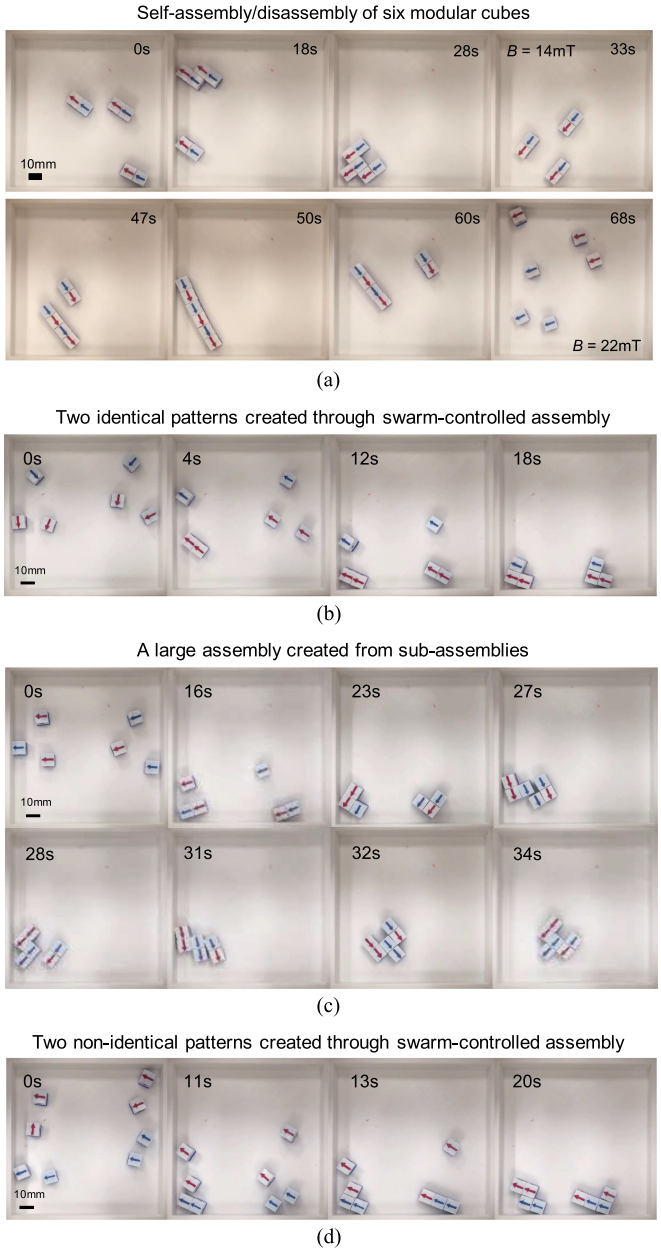

Fig. 6. Self-assembly and disassembly of modular subunits. (a) Six modular cubes assembled into three groups can be self-assembled, disassembled, and reassembled. (b) Six modular subunits, divided into two groups, are manipulated as swarms to create two assemblies of identical shapes. (c) Six modular subunits, divided into two groups, are manipulated to create a large assembly. (d) Eight modular subunits, divided into two groups, are manipulated to create two assemblies of nonidentical shapes. The magnitude of the magnetic flux density was normally 12 mT, but it was increased during disassembly operations.

IV. Reconfiguration of Modular Cubes

The concept of modular reconfiguration was explored through multiple experiments. The first consisted of changing the relative position of individual subunits in an assembled L-shape structure through partial disassembly and reassembly (Fig. 7). The second consisted of transforming the shape of the self-assembled configuration from an I-shape to an L-shape [Fig. 8(a)] and from an L-shape to a Z-shape [Fig. 8(b)]. Fig. 7 demonstrates position reconfiguration, where we change the order of cubes in a structure without changing the final assembly shape. First, we assigned a number to each cube, as shown in the top left corner of Fig. 7. Then, we performed partial disassembly (at

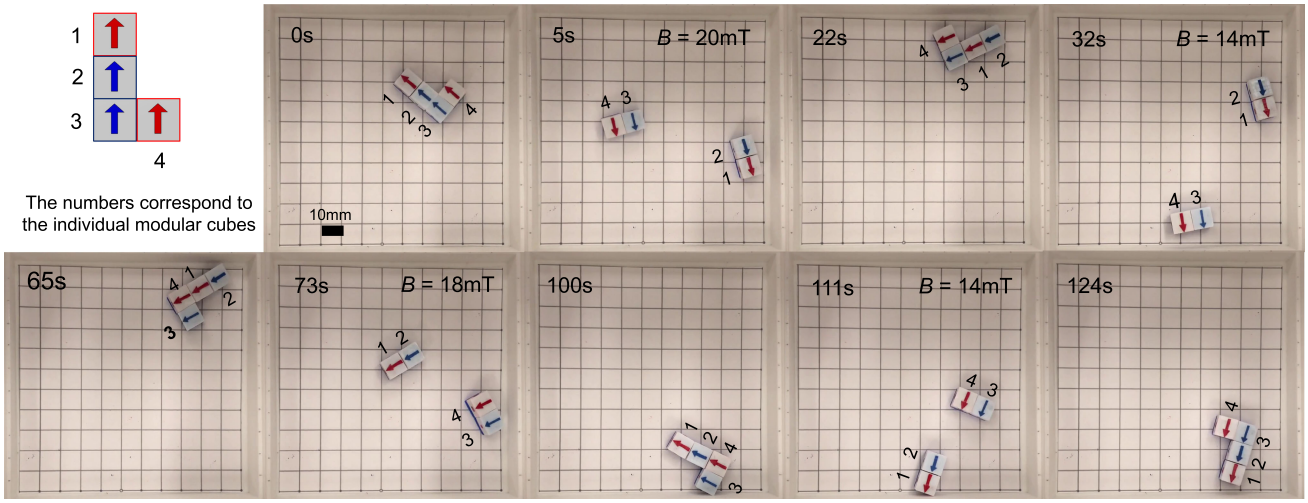

Fig. 7. Position reconfiguration of four modular cube subunits in an assembled L-shape configuration by changing relative positions of individual cubes in the L-shape (at 65 s) through partial disassembly, reconfiguration into an L-shape (at 22 and 100 s), and reassembly into the original L-shape configuration (at 124 s). The magnitude of the magnetic flux density was normally 12 mT, but it was increased during disassembly operations.

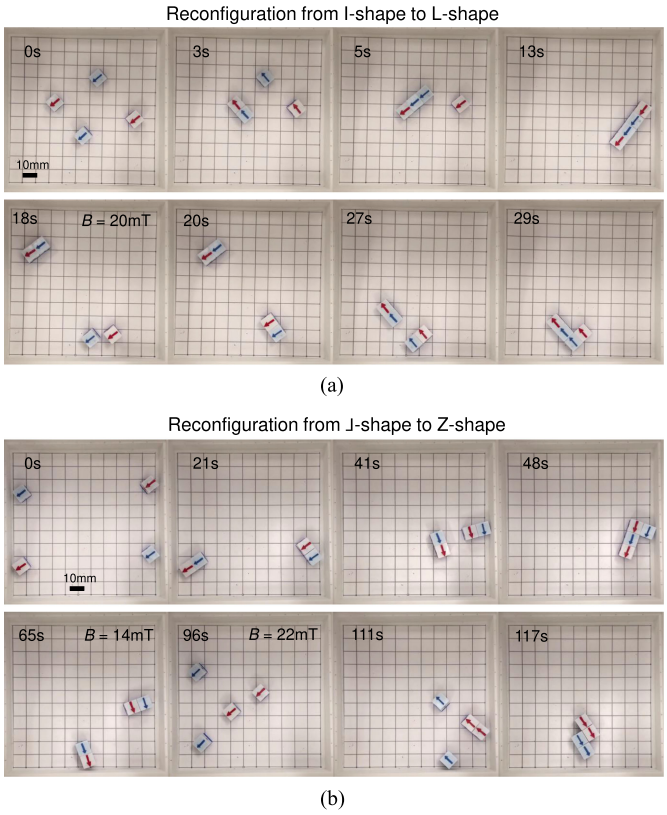

Fig. 8. Shape reconfiguration through self-assembly and disassembly of four modular subunits. (a) Four individual modular cubes are self-assembled into an I-shape through discrete motions and then reconfigured into an L-shape structure. (b) Four individual modular cubes are self-assembled in serial and parallel self-assembly to create an L-shape structure, disassembled, and reconfigured into a Z-shape structure. The magnitude of the magnetic flux density was normally 12 mT, but it was increased during disassembly operations.

5, 32, 73, and 111 s), kept track of the individual cubes being identified by the specific numbers, and performed reassembly (at 22, 65, 100, and 124 s). This process changed the relative positions of the blue and red cubes in the L-shapes (compare at 0 and 65 s) and in the L-shapes (compare at 22 and 100 s). However, the final self-assembled L-shape was the same as that in the beginning (compare at 0 and 124 s). This reconfiguration technique could be used with heterogeneous cubes to release therapeutic material, expose tools, or take samples.

Fig. 8(a) shows self-assembly of four individual modular cubes to form an I-shaped structure (at 13 s). Then, the structure was disassembled partially so that a part of the serial self-assembly was transformed into a parallel self-assembly (from 18 to 20 s). This partial disassembly enabled the cubes to be reassembled into an L-shape configuration (at 29 s). Similarly, as shown in Fig. 8(b), a transformation between configurations having different shapes (L-shape to Z-shape) was accomplished. The first part of the self-assembly process was similar to the previous one; however, the assembly occurred in a different sequence than before and created an L-shape [compare Fig. 8(a) at 29 s and Fig. 8(b) at 48 s]. Later, the subunits were completely disassembled in two steps (at 65 and 96 s) and then reconfigured into a Z-shape structure at 117 s, as shown in Fig. 8(b). These experiments demonstrate that our magnetic modular cube system can successfully achieve reconfigurability following preprogrammed input signals and controlled paths.

V. Motion Planner for Modular Cubes

The magnetic modular cubes described in this article open exciting opportunities for swarm control laws and algorithms. We manipulate modular cubes through controlled self-assembly and disassembly processes toward targeted, task-specific configurations in 2-D. Previous demonstrations show that these cubes can be made in large numbers, actuated by a uniform external magnetic field, interact with obstacles, combine if mating surfaces are brought in close proximity, and be split predictably by quickly rotating the magnetic field. Due to the magnetic modular cubes' cubic design, magnetically connected structures of these cubes are polyominoes in 2-D. *Polyominoes*

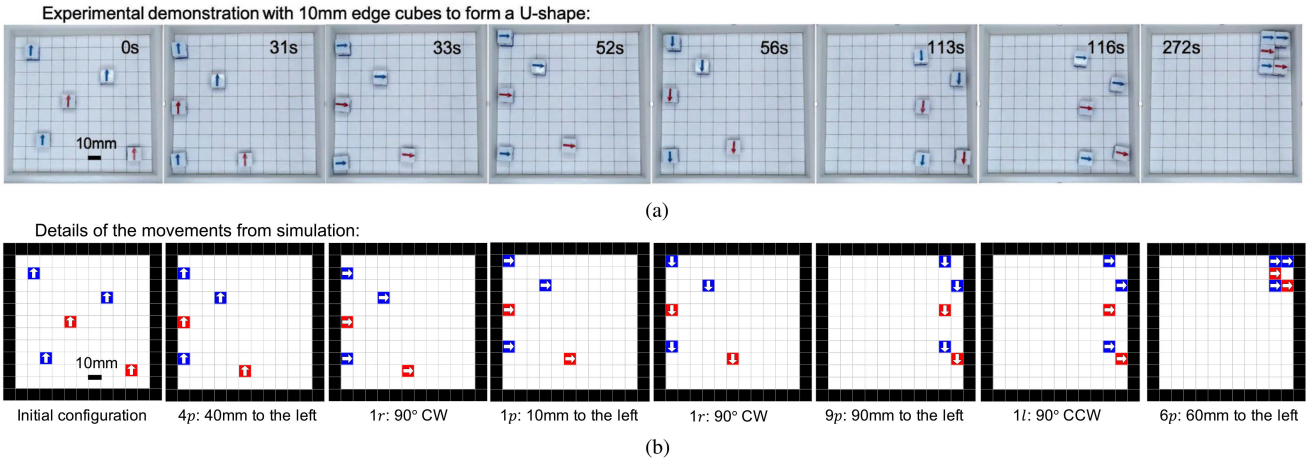

Fig. 9. Experimental demonstration and the corresponding 2-D simulator as five cubes with 10-mm edges form a U-shape. (a) Video snapshots from the hardware experiment. The magnitude of the magnetic flux density was kept constant at 12 mT throughout the experiment. (b) Details of movements from the simulation. See the attachment for videos of the demonstration.

are face-connected sets of unit squares that lie on the square grid graph. The motion planner computes all the polyomino shapes reachable from a given initial configuration and provides the shortest movement sequence to form each reachable shape. Obstacle-guided swarm control algorithms were developed and implemented for deterministic self-assembly processes.

We designed the simulator using a bounded 11×11 workspace based on the hardware experiment environment. Axis-aligned, unit-length squares represent all cubes. To aid in visual identification, the entire squares are colored. A red square represents a red cube and a blue square represents a blue cube. Arrows on the squares indicate the direction of the net magnetization (from magnetic south pole to north pole). Fig. 9 shows an experimental demonstration, and the corresponding 2-D simulator as five cubes forms a U-shape. To improve consistency between the experiment and simulation, cubes were actuated using pivot walking roughly moving in a straight line [at 31, 52, and 113 s in Fig. 9(a)] and applied in-place rotations [at 33, 56, and 116 s in Fig. 9(a)]. These cubes can be self-assembled when the distance between two faces of cubes with opposite magnetic poles becomes less than the half of their edge length during pivot walking [Fig. 9(a) from 116 to 272 s]. The simulator is more strict in modeling assembly events and only connects cubes with compatible magnetic bonds if they share an edge [see Fig. 9(b)].

Given a desired target polyomino and initial configuration of cubes, our motion planner has two parts: 1) use the 2-D simulator to compute all reachable polyomino configurations (and their shortest movement sequences) from the initial configuration; 2) if the target polyomino is unreachable, we disassemble and/or scramble the cubes and repeat part 1).

A. Self-Assembly Algorithm

Our self-assembly algorithm, Algorithm 1, takes as input the initial configuration and returns all reachable polyominoes and their shortest construction sequence. The main challenge in the self-assembly algorithm is the exponential growth of possible configurations as the number of modules increases. It is crucial to take some measures to prune the search tree. We assume that all modular subunits move at the same speed in the same direction unless they encounter a fixed obstacle. We restrict movement to include only pivot walking and in-place rotations. Pivot walking can only move modules perpendicular to the direction of net magnetization; so we limit the movement directions to port or starboard (left or right).

We define the north pole of each cube as the local front direction. All translation steps are based on the local front direction. At each step, cubes can move one unit length (10 mm) to the left (p for port) or right (s for starboard) or rotate in-place clockwise (r to the right) a quarter-turn or counterclockwise (l to the left) a quarter-turn [see Fig. 10(a), bottom]. We call a string of these moves a *motion sequence*. The motion sequence "$4p$, $1r$, $1p$, $1r$, $9p$, $1l$, $6p$" in Fig. 9(b) constructs a U-shape. We use a breadth-first search (BFS) algorithm to discover the reachable cube configurations. BFS is complete, but the search space size is exponential in the number of cubes; so we must prune the search tree aggressively. One way we prune this search is by not allowing movements that directly undo the previous input (e.g., no $\{r, l\}$ or $\{s, p\}$ sequences are allowed). The root of the search is the initial configuration, and we maintain a list of all unique relative configurations that have been reached. A *relative configuration* is represented by rotating the coordinate frame so that the magnetic north points up and then translating all cubes; so they touch the $x = 0$ and $y = 0$ boundaries of the workspace. The leaves of the search tree are either polyominoes or configurations that only lead to configurations reachable by a shorter path.

To further prune the tree, we only switch direction if the relative configuration of the cubes changes. When the relative configuration changes, we call this an *intermediate configuration*. Intermediate configurations occur when at least one cube (but not all cubes) strikes an obstacle. When this occurs, the new relative configuration is compared to the list and is only

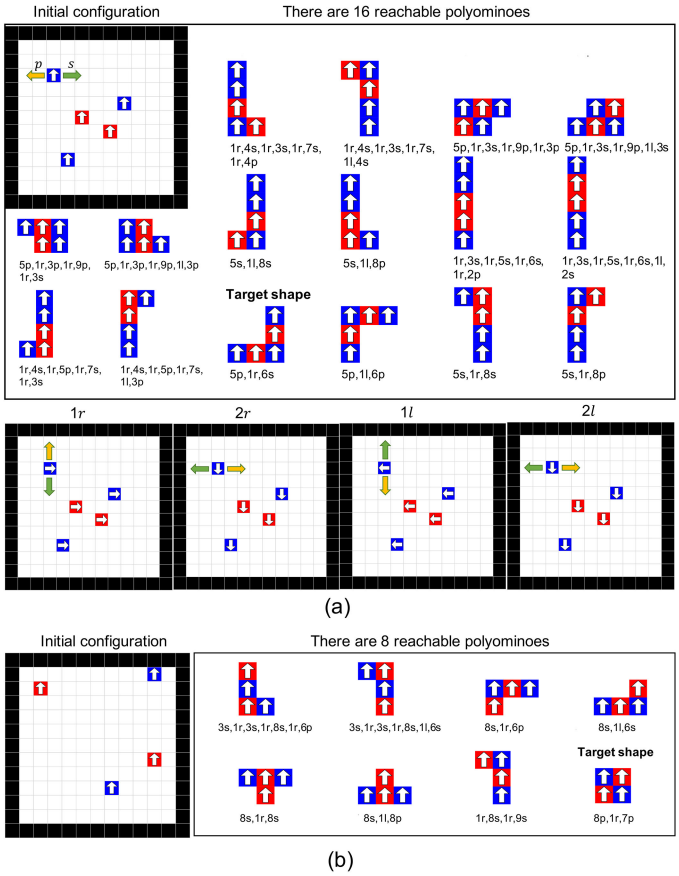

Fig. 10. Self-assembly results for two initial configurations. (a) Self-assembly results with three blue and two red cubes (top), and translation and rotation rules (bottom). (b) Self-assembly results with two red and two blue cubes.

appended if it is unique. After the polyomino is assembled, we compare the paths taken to save the shortest step sequence to construct the structure.

Fig. 10(a) shows the self-assembly result with three blue and two red cubes from an arbitrary initial configuration. Underneath each polyomino is listed the shortest step sequence to construct it. This shortest path information is stored in the tree structure. Fig. 10(b) shows the self-assembly result with two red and two blue cubes. Eight reachable polyominoes can be constructed from this initial configuration.

B. Applying the Motion Planner in Open Loop

To test the functionality of the motion planner, we selected the L-shape from Fig. 10(a) and the square shape from Fig. 10(b) as target shapes and applied the motion planner in an open-loop control. All cubes are represented by unit-length squares in the motion planner, but the movement sequences can also be applied for smaller cube sizes. Fig. 11 shows the comparison between the motion-planner and hardware experiment (with two sizes of modular cubes) to form the target L-shape from Fig. 10(a). The same open-loop control sequence (with scaled linear movements) was applied for two cube sizes (cubes with 10- and 2.8-mm edges). The shortest movement sequences found from the motion planner is "5p, 1r, 6s," which means five unit

Algorithm 1: CALCULATEREACHABLEPOLYS (c_0).

Result: S, set of reachable polyominoes
$S \leftarrow \{\}$
$C \leftarrow \{c_0\}$ `// List of all unique configurations`
$i \leftarrow 0$ `// current pointer`
$T[i] \leftarrow \{c_0, \varnothing, \varnothing\}$ `// add root node to BFS tree`
`// each node is {configuration, move, parent}`
$e \leftarrow i$ `// pointer to end of list`
while $i \leq e$ **do**
  $\{c_i, m_i, \text{parent}\} \leftarrow T[i]$
  moves $\leftarrow \{p, s, r, l\} \setminus \overline{m_i}$ `// Remove` m_i`'s inverse`
  for $m_j \in$ *moves* **do**
    $c_j = \text{APPLYMOVE}(c_i, m_j)$
    if $c_j \notin C$ **then**
      $C = \text{APPEND}(C, c_j)$
      $e \leftarrow e + 1$
      $T[e] \leftarrow \{c_j, m_j, i\}$
      if $\text{ISPOLYOMINO}(c_j)$ **then**
        $S = \text{APPEND}(S, c_j)$
  $i \leftarrow i + 1$

moves (50 mm) left, then rotate 90° clockwise, and then six unit moves (60 mm) to the right.

The number of pivot walking cycles required depends on the size of the cube. In the hardware experiment, after one cycle of pivot walking, cubes with 10-mm edges can move 6.29 ± 0.36 mm, while cubes with 2.8-mm edges can move 2.09 ± 0.07 mm. Therefore, the required number of pivot walking cycles to move 5p for cubes with 10-mm edges is 50/6.29 mm ≈ 8 cycles and for cubes with 2.8-mm edges is 50/2.09 mm ≈ 25 cycles.

There are small discrepancies between simulation and the experiment. In Fig. 11(b) at 85 s, the blue and red cubes were prematurely self-assembled, as they were brought in close proximity due to a slight path deviation of the blue cube during pivot walking. However, the assemblies could still continue following the paths from the motion planner to form the target L-shape. No premature self-assembly was evident when the smaller cubes (with 2.8-mm edges) followed the same path [see Fig. 11(c)]. After constructing the L-shape, the self-assembled structure could also be moved in the workspace by pivot walking and in-place rotations both in the motion planner and the hardware experiment [from 218 to 265 s in Fig. 11(b)]. The rolling motion [at 428 s in Fig. 11(c)] is not implemented in the 2-D simulator.

Fig. 12 uses the motion planner to form the target square shape in Fig. 10(b). The shortest movement sequence found by the motion planner is "8p, 1r, 7p," as shown in Fig. 12(a). To verify the results from the motion planner, first, four individual modular cubes were moved 8p (80 mm to the left) by pivot walking. The red cubes reached the target locations, but the blue cubes deviated slightly from a straight-line path [at 50 s in Fig. 12(b)]. Then, we applied a 90° clockwise in-place rotation to the cubes and continued pivot walking the cubes, until they moved seven units to the left to form the target square-shape (from 52 to 132 s). The path deviation by the blue cubes during pivot walking did not affect the end result. The self-assembled square shape

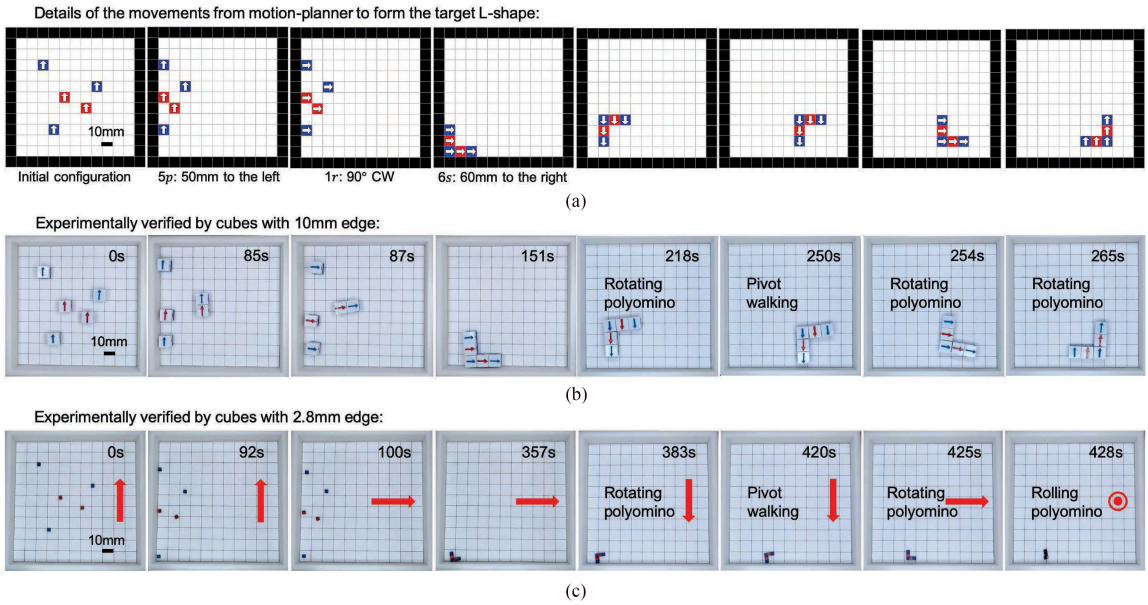

Fig. 11. Controlled self-assembly to form the target L-shape. (a) Details of movements from the motion planner. (b) Video snapshots showing open-loop implementation of the motion sequence using cubes with 10-mm edges. (c) Video snapshots showing details of movements from the experiment using cubes with 2.8-mm edges. The red arrow indicates the direction of the net magnetization. The magnitude of the applied magnetic flux density was kept constant at 12 mT throughout the experiments. See the attachment for videos of these demonstrations.

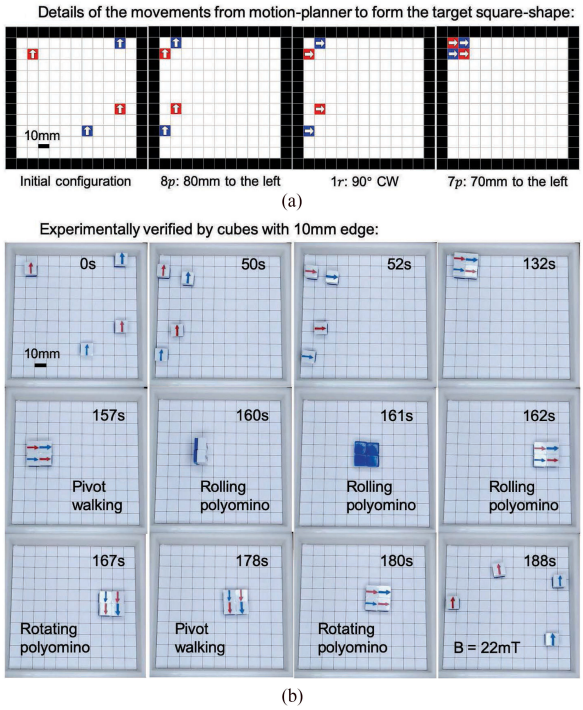

Fig. 12. Controlled self-assembly to form the target square shape. (a) Details of movements from the motion planner. (b) Video snapshots of hardware experiment. The magnitude of the magnetic flux density was normally 12 mT, but it was increased during disassembly operations. See the attachment for videos of the demonstration.

can be further actuated using pivot walking (from 132 to 157 s), rolling motion (from 157 to 162 s), and in-place rotations (at 167 and 180 s). Finally, the self-assembled modular structure could be completely disassembled into individual modular subunits (at 188 s) by following the disassembly mechanism described in Section III. The strength of the magnetic flux applied for the disassembly was 22 mT.

C. Disassembly: Assembling Unreachable Polyominoes

The set of polyomino shapes that can be made depends on the number of cubes and their colors. For example, with four cubes without colors, there are 19 fixed polyominoes [38] including L-shapes, Z-shapes, I-shapes, T-shapes, and square shapes, but they are not magnetically connected. Based on our cubes' design, a set of all red (or all blue) cubes can only make serially connected I-shapes (top arrows aligned tip-to-tail), and square shapes require two red and two blue cubes [see Fig. 12(b) at 132 s].

Our code computes the set of polyominoes that can be constructed from a given set of cubes. Often, some of these polyominoes are unreachable from a given initial configuration. Moreover, repeated tests with random initial configurations show that some polyominoes are reachable more often than others. This makes some polyominoes harder to construct. Given a target polyomino, a reasonable first step is to choose a set of cubes that maximize the frequency that the target polyomino is reachable. One method to enable constructing arbitrary polyominoes is to add engineered obstacles into the workspace and use them to rearrange cubes [39]–[41]. These obstacles are not required. This article chooses to use an obstacle-free, square workspace. If the desired polyomino is unreachable from a given initial configuration, one can repeatedly generate new initial configurations until the polyomino is reachable. Rapidly rotating the magnetic field is one way to separate and scramble the cubes into new configurations.

Fig. 13 shows results from an experiment using one blue and three red cubes with 2.8-mm edges. The cubes were combined

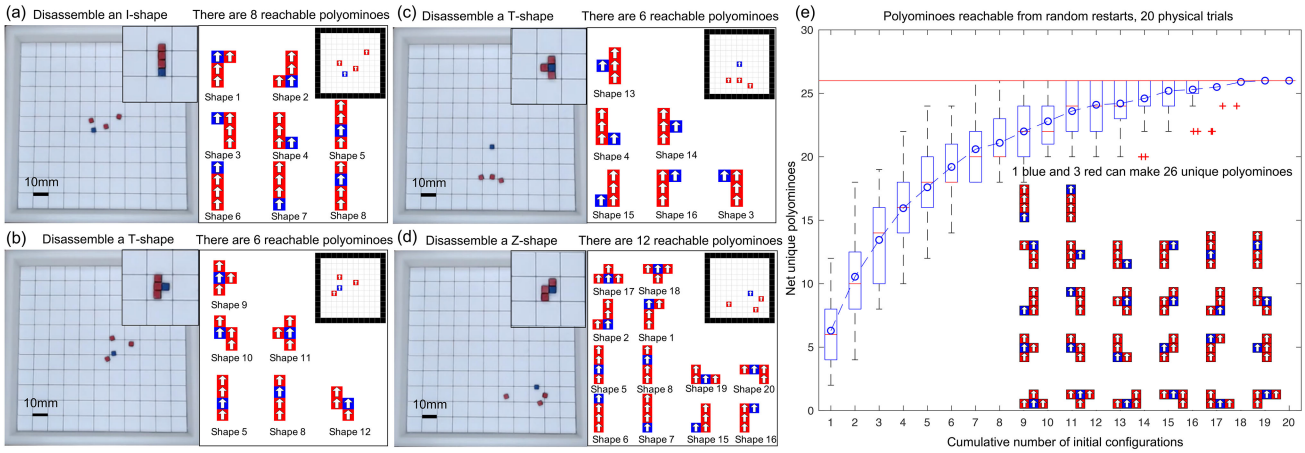

Fig. 13. Disassembly results. (a) to (d) Four initial configurations before (inset image) and after disassembly using cubes with 2.8-mm edges, and the polyominoes reachable from these disassembled configurations. (e) Statistical results from 20 of these physical trials. The red line is the maximum number of possible configurations (26). Red + signs show outliers. See the attachment for videos of these demonstrations.

into a polyomino and then dissembled by rapidly rotating the magnetic field. After each disassembly event, we computed the set of reachable polyominoes. Fig. 13(a) (left) shows an example of disassembling an I-shape (top right corner). The motion planner takes the configuration after disassembly as the initial configuration [Fig. 13(a), right black box] and computes the number of reachable polyominoes. Eight reachable polyominoes can be generated, including L-shapes and I-shapes. Fig. 13(b) and (c) shows disassembly results for two T-shapes with different cube arrangements and the number of reachable polyominoes that could be generated from each disassembled configuration. T-shapes and Z-shapes are reachable. Fig. 13(d) shows an example of disassembling a Z-shape. In total, 20 unique polyominoes could be generated from these four initial configurations.

However, one blue and three red cubes can make 26 unique polyominoes. These 26 shapes are shown in Fig. 13(e). Constructing all 26 requires additional randomization of the cubes. We repeated the experiment 20 times. The median number of reachable polyominoes after one disassembly is 6. After disassembling the cubes twice, the median number of reachable polyominoes is 10. After disassembling the cubes 19 times, it is possible to reach all 26 polyominoes.

VI. Conclusion

The modular robotic platform presented in this article has a simple, economic, and scalable design. It is actuated through discrete motion modes, is wirelessly controlled, has a robust assembly–disassembly capability, is reconfigurable, and shows reproducible behavior. Moreover, all modules can be commanded in parallel and the same commands can actuate individual modules and assemblies of modules. These qualities are pertinent to mesoscale manufacturing and require no motors, sensors, batteries, or computation. Through experiments and computational modeling, we showed the versatility of our modular robotic platform at performing assembly–disassembly and reconfiguration. The pivot walking motion mechanism is effective for performing 2-D manipulation. The rolling motion could be essential for 3-D manipulation and will be explored in future work. The on-board magnetic coupling mechanism makes the assembly process self-driven. Our motion-planner can be used to construct the desired polyomino shapes, and the same planner is effective for cubes with 2.8-mm edges and cubes with 10-mm edges.

Future work should focus on making a high-fidelity simulator for motion planning, modeling the disassembly process, and increasing the complexity of the self-assembly/disassembly by using more cubes and by 3-D construction.

Multimedia Materials

Included with the manuscript are videos for the modular cubes' motion modes and play-by-plays of the experiments. Interested readers are encouraged to reach out to the corresponding authors for more information regarding these results.

Acknowledgment

The authors would like to thank Caitlin Bubel and Meyer Willson for helping with preliminary experiments and Louis W. Rogowski and Hoyeon Kim for constructing the Helmholtz coil system.

References

[1] J. Bishop *et al.*, "Programmable parts: A demonstration of the grammatical approach to self-organization," in *Proc. IEEE/RSJ Int. Conf. Intell. Robots Syst.*, 2005, pp. 3684–3691.

[2] J. Liu, X. Zhang, and G. Hao, "Survey on research and development of reconfigurable modular robots," *Adv. Mech. Eng.*, vol. 8, no. 8, pp. 1–21, 2016.

[3] S. Chennareddy, A. Agrawal, and A. Karuppiah, "Modular self-reconfigurable robotic systems: A survey on hardware architectures," *J. Robot.*, vol. 2017, no. 2, pp. 1–19, 2017.

[4] M. Yim, Y. Zhang, and D. Duff, "Modular robots," *IEEE Spectr.*, vol. 39, no. 2, pp. 30–34, Feb. 2002.

[5] U. K. Cheang, F. Meshkati, H. Kim, K. Lee, H. C. Fu, and M. J. Kim, "Versatile microrobotics using simple modular subunits," *Sci. Rep.*, vol. 6, 2016, Art. no. 30472.

[6] J. Lengiewicz and P. Hołobut, "Efficient collective shape shifting and locomotion of massively-modular robotic structures," *Auton. Robots*, vol. 43, no. 1, pp. 97–122, 2019.
[7] M. Sitti *et al.*, "Biomedical applications of untethered mobile milli/microrobots," *Proc. IEEE*, vol. 103, no. 2, pp. 205–224, Feb. 2015.
[8] S. Tasoglu, C. Yu, H. Gungordu, S. Guven, T. Vural, and U. Demirci, "Guided and magnetic self-assembly of tunable magnetoceptive gels," *Nat. Commun.*, vol. 5, 2014, Art. no. 4702.
[9] H. Xie *et al.*, "Reconfigurable magnetic microrobot swarm: Multimode transformation, locomotion, and manipulation," *Sci. Robot.*, vol. 4, no. 28, 2019, Art. no. eaav8006.
[10] R. Pelrine, A. Wong-Foy, A. Hsu, and B. McCoy, "Self-assembly of millis-cale robotic manipulators: A path to highly adaptive, robust automation systems," in *Proc. Int. Conf. Manipulation, Autom. Robot. Small Scales*, 2016, pp. 1–6.
[11] P. J. White and M. Yim, "Scalable modular self-reconfigurable robots using external actuation," in *Proc. IEEE/RSJ Int. Conf. Intell. Robots Syst.*, 2007, pp. 2773–2778.
[12] W. Saab, P. Racioppo, and P. Ben-Tzvi, "A review of coupling mechanism designs for modular reconfigurable robots," *Robotica*, vol. 37, no. 2, pp. 378–403, 2019.
[13] B. J. Nelson, I. K. Kaliakatsos, and J. J. Abbott, "Microrobots for minimally invasive medicine," *Annu. Rev. Biomed. Eng.*, vol. 12, pp. 55–85, 2010.
[14] J. J. Abbott, E. Diller, and A. J. Petruska, "Magnetic methods in robotics," *Annu. Rev. Control. Robot. Auton. Syst.*, vol. 3, no. 1, pp. 57–90, 2020.
[15] J. W. Romanishin, K. Gilpin, and D. Rus, "M-blocks: Momentum-driven, magnetic modular robots," in *Proc. IEEE/RSJ Int. Conf. Intell. Robots Syst.*, 2013, pp. 4288–4295.
[16] U. A. Fiaz and J. S. Shamma, "usBot: A modular robotic testbed for programmable self-assembly," *IFAC-PapersOnLine*, vol. 52, no. 15, pp. 121–126, 2019.
[17] J. Davey, N. Kwok, and M. Yim, "Emulating self-reconfigurable robots-design of the SMORES system," in *Proc. IEEE/RSJ Int. Conf. Intell. Robots Syst.*, 2012, pp. 4464–4469.
[18] K. Gilpin, K. Kotay, D. Rus, and I. Vasilescu, "Miche: Modular shape formation by self-disassembly," *Int. J. Robot. Res.*, vol. 27, nos. 3-4, pp. 345–372, 2008.
[19] S. Murata, E. Yoshida, A. Kamimura, H. Kurokawa, K. Tomita, and S. Kokaji, "M-TRAN: Self-reconfigurable modular robotic system," *IEEE/ASME Trans. Mechatronics*, vol. 7, no. 4, pp. 431–441, Dec. 2002.
[20] H. Kurokawa, A. Kamimura, E. Yoshida, K. Tomita, S. Kokaji, and S. Murata, "M-TRAN II: metamorphosis from a four-legged walker to a caterpillar," in *Proc. IEEE/RSJ Int. Conf. Intell. Robots Syst.*, 2003, pp. 2454–2459.
[21] E. Diller, S. Floyd, C. Pawashe, and M. Sitti, "Control of multiple heterogeneous magnetic microrobots in two dimensions on nonspecialized surfaces," *IEEE Trans. Robot.*, vol. 28, no. 1, pp. 172–182, Feb. 2012.
[22] H. Gu, Q. Boehler, D. Ahmed, and B. J. Nelson, "Magnetic quadrupole assemblies with arbitrary shapes and magnetizations," *Sci. Robot.*, vol. 4, no. 3, 2019, Art. no. eaax8977.
[23] E. Diller, C. Pawashe, S. Floyd, and M. Sitti, "Assembly and disassembly of magnetic mobile micro-robots towards deterministic 2-D reconfigurable micro-systems," *Int. J. Robot. Res.*, vol. 30, no. 14, pp. 1667–1680, 2011.
[24] B. T. Kirby *et al.*, "A modular robotic system using magnetic force effectors," in *Proc. IEEE/RSJ Int. Conf. Intell. Robots Syst.*, 2007, pp. 2787–2793.
[25] B. R. Donald, C. G. Levey, and I. Paprotny, "Planar microassembly by parallel actuation of MEMS microrobots," *J. Microelectromech. Syst.*, vol. 17, no. 4, pp. 789–808, 2008.
[26] R. Pfeifer, M. Lungarella, and F. Iida, "Self-organization, embodiment, and biologically inspired robotics," *Science*, vol. 318, no. 5853, pp. 1088–1093, 2007.
[27] K. Tomita, S. Murata, H. Kurokawa, E. Yoshida, and S. Kokaji, "Self-assembly and self-repair method for a distributed mechanical system," *IEEE Trans. Robot. Autom.*, vol. 15, no. 6, pp. 1035–1045, Dec. 1999.
[28] Z. Butler, K. Kotay, D. Rus, and K. Tomita, "Generic decentralized control for lattice-based self-reconfigurable robots," *Int. J. Robot. Res.*, vol. 23, no. 9, pp. 919–937, 2004.
[29] R. Fitch and Z. Butler, "Million module march: Scalable locomotion for large self-reconfiguring robots," *Int. J. Robot. Res.*, vol. 27, nos. 3-4, pp. 331–343, 2008.
[30] F. Hurtado, E. Molina, S. Ramaswami, and V. Sacristán, "Distributed reconfiguration of 2D lattice-based modular robotic systems," *Auton. Robots*, vol. 38, no. 4, pp. 383–413, 2015.
[31] A. A. Gorbenko and V. Y. Popov, "Programming for modular reconfigurable robots," *Program. Comput. Soft.*, vol. 38, pp. 13–23, 2012.
[32] J. W. Suh, S. B. Homans, and M. Yim, "Telecubes: Mechanical design of a module for self-reconfigurable robotics," in *Proc. IEEE Int. Conf. Robot. Autom.*, 2002, pp. 4095–4101.
[33] S. Miyashita, S. Guitron, M. Ludersdorfer, C. R. Sung, and D. Rus, "An untethered miniature origami robot that self-folds, walks, swims, and degrades," in *Proc. IEEE Int. Conf. Robot. Autom.*, 2015, pp. 1490–1496.
[34] O. Youssefi and E. Diller, "Dry surface micromanipulation using an untethered magnetic microrobot," in F. Janabi-Sharifi and W. Melek Eds., *Adv. Motion Sens. Control Robotic Appl.*, Lecture Notes in Mechanical Engineering. Springer, Cham, 2019, pp. 75–91.
[35] E. Al Khatib, A. Bhattacharjee, P. Razzaghi, L. W. Rogowski, M. J. Kim, and Y. Hurmuzlu, "Magnetically actuated simple millirobots for complex navigation and modular assembly," *IEEE Robot. Autom. Lett.*, vol. 5, no. 2, pp. 2958–2965, Apr. 2020.
[36] C. Bi, M. Guix, B. V. Johnson, W. Jing, and D. J. Cappelleri, "Design of microscale magnetic tumbling robots for locomotion in multiple environments and complex terrains," *Micromachines*, vol. 9, no. 2, 2018, Art. no. 68.
[37] Y. Lu, A. Bhattacharjee, D. Biediger, M. J. Kim, and A. T. Becker, "Enumeration of polyominoes & polycubes composed of magnetic cubes," in *Proc. IEEE/RSJ Int. Conf. Intell. Robots Syst.*, Prague, Czech Republic, 2021.
[38] D. H. Redelmeier, "Counting polyominoes: Yet another attack," *Discrete Math.*, vol. 36, no. 2, pp. 191–203, 1981.
[39] S. Manzoor, S. Sheckman, J. Lonsford, H. Kim, M. J. Kim, and A. T. Becker, "Parallel self-assembly of polyominoes under uniform control inputs," *IEEE Robot. Autom. Lett.*, vol. 2, no. 4, pp. 2040–2047, Oct. 2017.
[40] A. Schmidt, S. Manzoor, L. Huang, A. T. Becker, and S. P. Fekete, "Efficient parallel self-assembly under uniform control inputs," *IEEE Robot. Autom. Lett.*, vol. 3, no. 4, pp. 3521–3528, Oct. 2018.
[41] J. Balanza-Martinez *et al.*, "Full tilt: Universal constructors for general shapes with uniform external forces," in *Proc. 30th Annu. ACM-SIAM Symp. Discrete Algorithms*, 2019, pp. 2689–2708.

Anuruddha Bhattacharjee received the B.S. degree in mechanical engineering from the Bangladesh University of Engineering and Technology, Dhaka, Bangladesh, in 2017. He is currently working toward the Ph.D. degree in mechanical engineering with Southern Methodist University, Dallas, TX, USA.

His research focuses on fabrication, dynamics, control, and manipulation of modular reconfigurable robots for *in-situ* manufacturing at the mesoscale and bio-inspired soft-robots for *in-vivo* applications.

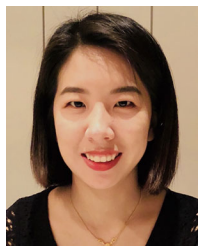

Yitong Lu received the M.S. degree in electrical and computer engineering from the New Jersey Institute of Technology, Newark, NJ, USA, in 2019. She is currently working toward the Ph.D. degree in electrical and computer engineering with the University of Houston, Houston, TX, USA.

She is involved in studies of magnetic manipulation of magnetic swimmers for blood clot removal and 3-D path-following, control for robotics applications, and motion planning algorithms for magnetic modular robots.

Aaron T. Becker (Senior Member, IEEE) received the M.S. and Ph.D. degrees in electrical and computer engineering from the University of Illinois, Urbana-Champaign, IL, USA, in 2008 and 2012, respectively.

He is currently an Associate Professor with the Electrical and Computer Engineering Department, University of Houston, Houston, TX, USA. He was a Postdoctoral Research Scholar with the Multi-robot Systems Lab, Rice University, Houston, and with Boston Children's Hospital & Harvard Medical School, Boston, MA, USA.

Dr. Becker was the Recipient of the Best Paper Award at *IEEE/RSJ International Conference on Intelligent Robots and Systems (IROS)* in 2014 and the NSF CAREER Award in 2016.

MinJun Kim (Senior Member, IEEE) is currently the Robert C. Womack Endowed Chair Professor of Engineering with the Department of Mechanical Engineering, Southern Methodist University, Dallas, TX, USA. He received his B.S. and M.S. degrees in mechanical engineering from Yonsei University in Korea and Texas A&M University, respectively. Dr. Kim completed his Ph.D. degree in engineering at Brown University, where he held the prestigious Simon Ostrach Fellowship. Following his graduate studies, Dr. Kim was a postdoctoral research fellow in the Rowland Institute at Harvard University. He has been exploring biological transport phenomena including cellular/molecular mechanics and engineering in novel nano/microscale architectures to produce new types of nanobiotechnology, such as nanopore technology and nano/microrobotics.

Prof. Kim's notable awards include the National Science Foundation CAREER Award in 2008, the Human Frontier Science Program Young Investigator Award in 2009, the Army Research Office Young Investigator Award in 2010, and the Alexander von Humboldt Fellowship in 2011. He became a Fellow of ASME in 2014.